Spin-correlation transport and multiple resistive states in multiferroic tunnel junctions

Xiaolin Zhang,[1] Lei Yin,[1] Sicong Zhu,[2,3] Ruiqing Cheng,[1] Yao Wen,[1] and Jun He[1,4,*]

[1]*Key Laboratory of Artificial Micro- and Nano-Structures of Ministry of Education, and School of Physics and Technology, Wuhan University, Wuhan 430072, China*

[2]*Hubei Province Key Laboratory of Systems Science in Metallurgical Process, The State Key Laboratory for Refractories and Metallurgy, Collaborative Innovation Center for Advanced Steels, International Research Institute for Steel Technology, Wuhan University of Science and Technology, Wuhan 430081, China*

[3]*Department of Mechanical Engineering, National University of Singapore, 117575 Singapore*

[4]*Wuhan Institute of Quantum Technology, Wuhan 430206, China*

(Received 11 March 2024; revised 31 May 2024; accepted 15 July 2024; published 25 July 2024)

Multiferroic tunneling junctions (MFTJs), which comprise magnetic electrodes and extremely thin ferroelectric tunneling barriers, are promising contenders for nonvolatile memory applications. Noncollinear antiferromagnetic Mn_3Sn with time-reversal symmetry-breaking polarization properties and ferroelectric α-In_2Se_3 may open up the possibility of constructing room-temperature MFTJs. In this study, we investigate the spin-correlation transport in the MFTJs with $Mn_3Sn/BN/\alpha$-In_2Se_3/Mn_3Sn structure using first-principles calculations. The resistance in this structure can be manipulated by tuning the directions of both the Néel vector of Mn_3Sn and the electric polarization of the α-In_2Se_3 layer. Thus, multiple tunneling resistive states can be realized. We predict that huge tunneling magnetoresistance up to 6650% can be obtained by switching the magnetically oriented Néel vectors of Mn_3Sn, and more than 8000% tunneling electrical resistance can be obtained by controlling the ferroelectric structure of α-In_2Se_3. Our work underscores the potential applications of Mn_3Sn in multiferroic nonvolatile memories and lays the foundation for the development of ultrafast and efficient spintronic devices utilizing antiferromagnets.

DOI: 10.1103/PhysRevB.110.024428

I. INTRODUCTION

The rapid advancement of technologies such as big data, artificial intelligence, and the internet of things has generated an increasingly pressing need for data storage solutions with enhanced capacity, speed, and energy efficiency [1–7]. In response, different nonvolatile storage technologies [8–11], including magnetic tunnel junction memory devices [12–15], phase-change memory devices [16], ferroelectric memory devices [17,18], and memristors [19], have emerged, offering notable advantages in storage density, read/write speed, and power consumption. Multiferroic tunneling junctions (MFTJs)have garnered attention for their potential to drive the development of innovative magnetic memory devices. Through the controllable manipulation of the interaction between ferroelectric (FE) and ferromagnetic (FM) materials, MFTJs enable the realization of diverse resistive states, facilitating the storage and retrieval of information [20–22].

Antiferromagnetic (AFM) materials do not generate stray magnetic fields, so they have short switching times (resonance frequencies on the order of THz compared to GHz for ferromagnets), making them potentially valuable for applications in high-speed, high-density memory devices [23–28]. The Néel vector refers to a physical quantity that represents the direction of magnetic moments in AFM materials. Advancing the field of AFM spintronics necessitates the development of more sensitive and reliable methods for electrically detecting Néel vectors [29]. Spin-polarized currents generated by the spin-splitting Fermi surface of a noncollinear antiferromagnetic material (e.g., Mn_3Sn) can be exploited by driving currents that can be regulated by the corresponding orientation of the Néel vectors in the two AFM electrodes [30]. This method can provide a different means of electrical detection in the realm of AFM spintronics and is expected to play an important role in materials research and electronic device applications [31]. In noncollinear AFM materials, the Néel vector can be rotated in three dimensions without disappearing completely [32]. This unique characteristic renders noncollinear AFM materials highly promising for applications in magnetics and magnetoelectric devices aimed at high-density storage [33–36].

Mn_3Sn has a noncollinear AFM property, which implies that its magnetic moment directions show a noncollinear arrangement in space, a property that can provide additional freedom and flexibility for MFTJs [37–41]. Furthermore, the FM state can usually coexist with the FE state, which facilitates the construction of MFTJs [42–44]. Notably, a study led by Nakatsuji highlighted the potential of utilizing the Weyl semimetal Mn_3Sn to develop the next generation of high-speed storage devices [45]. That study found that the outer fermions in Mn_3Sn can exist in two possible states, which can be used to represent binary digits and can be controlled and switched by an external current. Additionally,

*Contact author: he-jun@whu.edu.cn

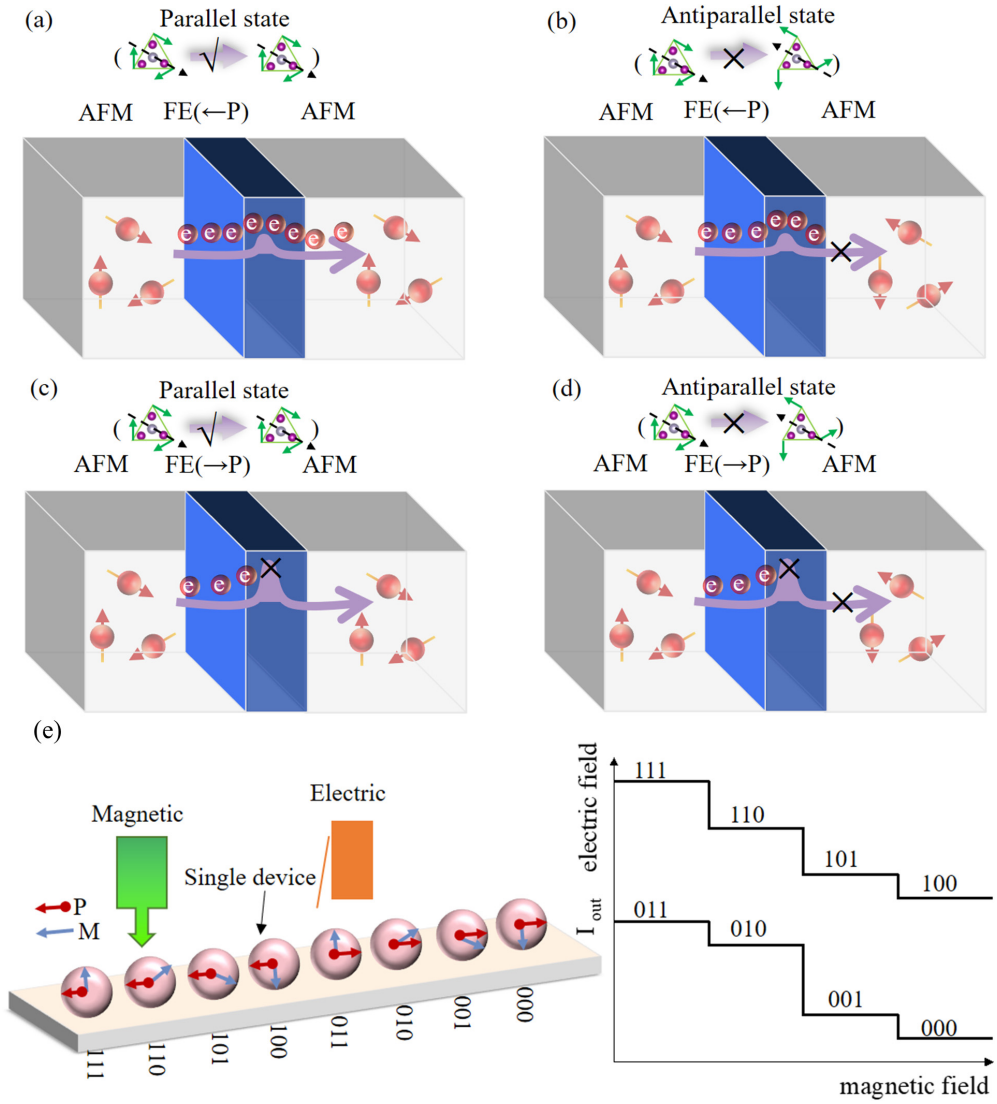

FIG. 1. Schematic diagram of the MFTJs based on AFM/FE/AFM structure. For the FE layer polarized to the left, the electron tunneling schematic diagrams of the (a) parallel configuration ($\alpha_L = 0°$, $\alpha_R = 0°$) and (b) antiparallel configuration ($\alpha_L = 0°$, $\alpha_R = 180°$); (c),(d) for the FE polarized to the right. (e) Schematic diagram of the manipulating resistive states for multilevel data storage in MFTJs. The blue arrows denote the relative angle of the Néel vector of left and right electrodes, and the red arrows represent polarization direction. Eight resistive states, enabling the achievement of three-bit storage, could be realized by tuning the magnetic and electric fields.

Mn_3Sn has excellent electrical properties and thermal stability, which are essential for achieving stable MFTJs [46]. Consequently, Mn_3Sn's noncollinear antiferromagnetic nature presents promising advantages for the construction of MFTJs.

In this study, we introduce a multiferroic model comprised of noncollinear AFM Mn_3Sn and FE α-In_2Se_3. Utilizing density functional theory (DFT) and conductivity calculations, we estimate multiple tunneling resistive states within the $Mn_3Sn/BN/\alpha$-In_2Se_3/Mn_3Sn heterostructure. The observed phenomenon is governed by the concurrent manipulation of the corresponding orientations of the Néel vectors in the left and right electrodes, as well as the distinct electric polarization directions of α-In_2Se_3. Leveraging the distinctive attributes of multiferroic devices, the transition between different states is achieved through electrical and magnetic control, thereby enabling high data density and low-energy multibit storage. This approach offers a reliable means of introducing additional degrees of freedom and flexibility to MFTJs.

II. RESULTS AND DISCUSSION

A. The principle achieving different resistive states in a single device

The electron transport across the tunnel barrier between two AFM electrodes should depend on the relative alignment of the Néel vectors of the electrodes, resulting in a high electron transmission rate and low resistance state [Figs. 1(a)–1(d)]. For misaligned Néel vectors, the electron transmission rate is lower, leading to a high resistance state. Additionally, for ferroelectric materials, theoretically, transitions between ferroelectric states can alter the barrier height, resulting in significant changes in the transmission rate. To achieve the objectives of multiferroics and ultimate memory within a single

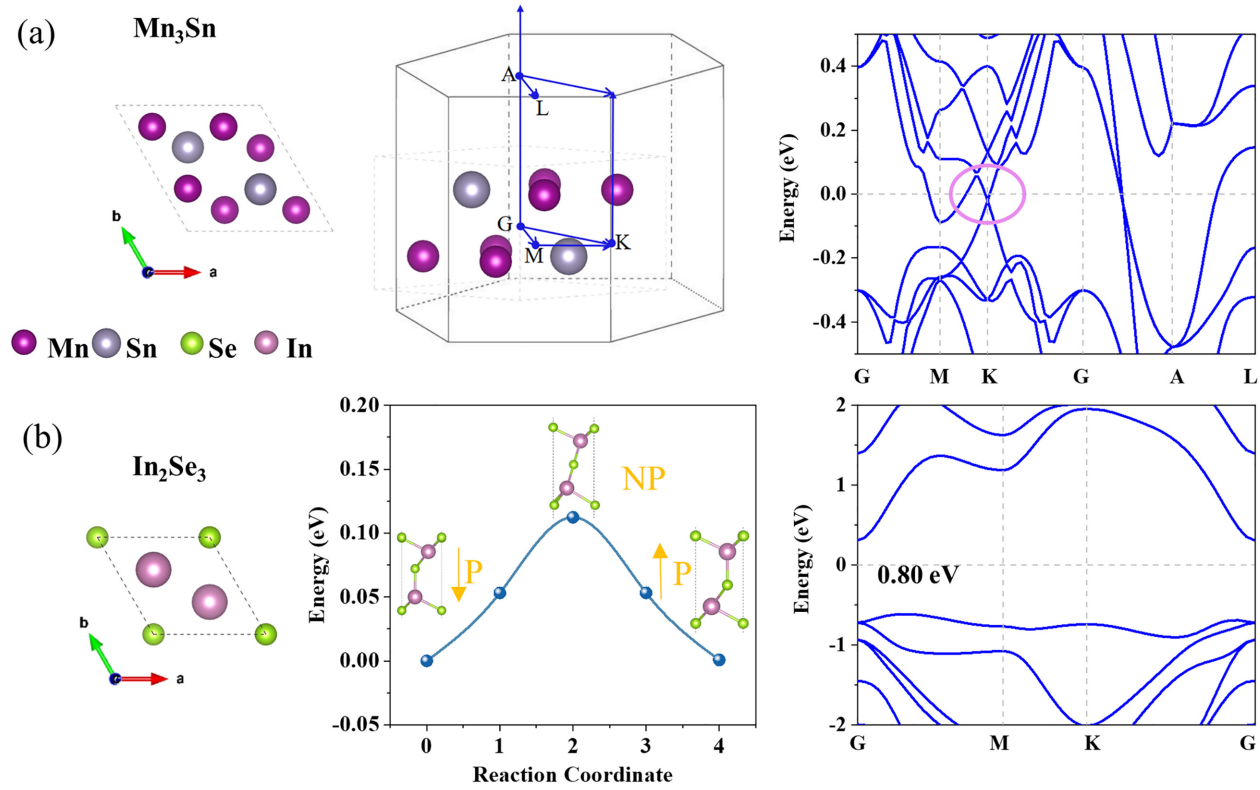

FIG. 2. (a) Atomic structure of bulk Mn_3Sn (left), as well as the corresponding Brillouin zone paths (middle) and band structure (right). (b) Atomic structure of monolayer α-In_2Se_3 (left), as well as the corresponding polarization direction switching paths calculated using the NEB direction for two different ferroelectric polarization configurations (middle) and band structure (right).

device, a framework is proposed herein, wherein multiferroic devices serve as the smallest storage units, systematically distributed throughout the system. As depicted in Fig. 1(e), multiferroic devices are represented by pink circles, where the blue arrows denote the relative angle of the Néel vector of left and right electrodes, and the red arrows represent polarization to the left or right, respectively. The Néel vector of the AFM magnetic moment encompasses only specific angles, necessitating eight distinct states to represent all possible combinations. By controlling the Néel vector of AFM materials with noncollinear left and right electrodes in the MFTJs and by controlling the polarization direction of the ferroelectric materials, a similar "ladderlike" arrangement of the eight resistive states can be realized. Since the eight resistive states can be stored in three bits, the highest resistive state corresponds to the binary number "000," the lowest resistive state corresponds to "111," and then the remaining six resistive states are mapped to the numbers "001" to "110," so that the corresponding three-digit binary number can be recognized and stored. The diversity of the resistive states is utilized to achieve multibit storage and improve storage density and information capacity. In practice, the stability and reliability of the resistive states need to be ensured to ensure that the different states are recognized and stored correctly.

B. Geometrical structure and magnetic properties

To verify the magnetic and electrical controllability of the above-mentioned multiresistive states, it is necessary to design a trilayer AFM/FE/AFM heterojunction. For the AFM layer and FE layer, we chose Mn_3Sn and α-In_2Se_3 as the candidate materials for this study. Mn_3Sn belongs to a group of alloys [Fig. 2(a)] with a special crystal structure and magnetic properties based on the experimental lattice parameters $a = b = 5.65$ Å and $c = 4.522$ Å. At room temperature, Mn_3Sn exhibits AFM behavior, transitioning to an FM state at lower temperatures, indicative of its unique magnetic structure. The calculated magnetic moment per Mn atom is approximately 3.12 μB, confined within the *XY* plane (for details of the calculations, see the Supplemental Material [47], and see also Refs. [48–51]). Contrary to a simple parallel (P) or antiparallel (AP) arrangement, the magnetic moment orientations within Mn_3Sn crystals demonstrate a complex noncollinear configuration within the *XY* plane. Bulk Mn_3Sn crystallizes in a layered hexagonal lattice with space group *P*63/*mmc*, and Fig. 2(a) shows the set of all possible states in momentum space that can be occupied by Mn_3Sn electrons in the hexagonal lattice structure. In the vicinity of these symmetry points, the energy band structure of the electrons displays special properties. The band structure of Fig. 2(a) clearly shows that there are band crossovers (Weyl point) near the Fermi level around the high symmetry *K* points, which may lead to some peculiar electron transport properties. α-In_2Se_3 ($a = 4.026$ Å) is a semiconducting material belonging to a group of layered compounds with inherent ferroelectric properties (the work function is shown Fig. S1 in the Supplemental Material [47]). Ferroelectric materials usually exhibit the property of polarization under an electric

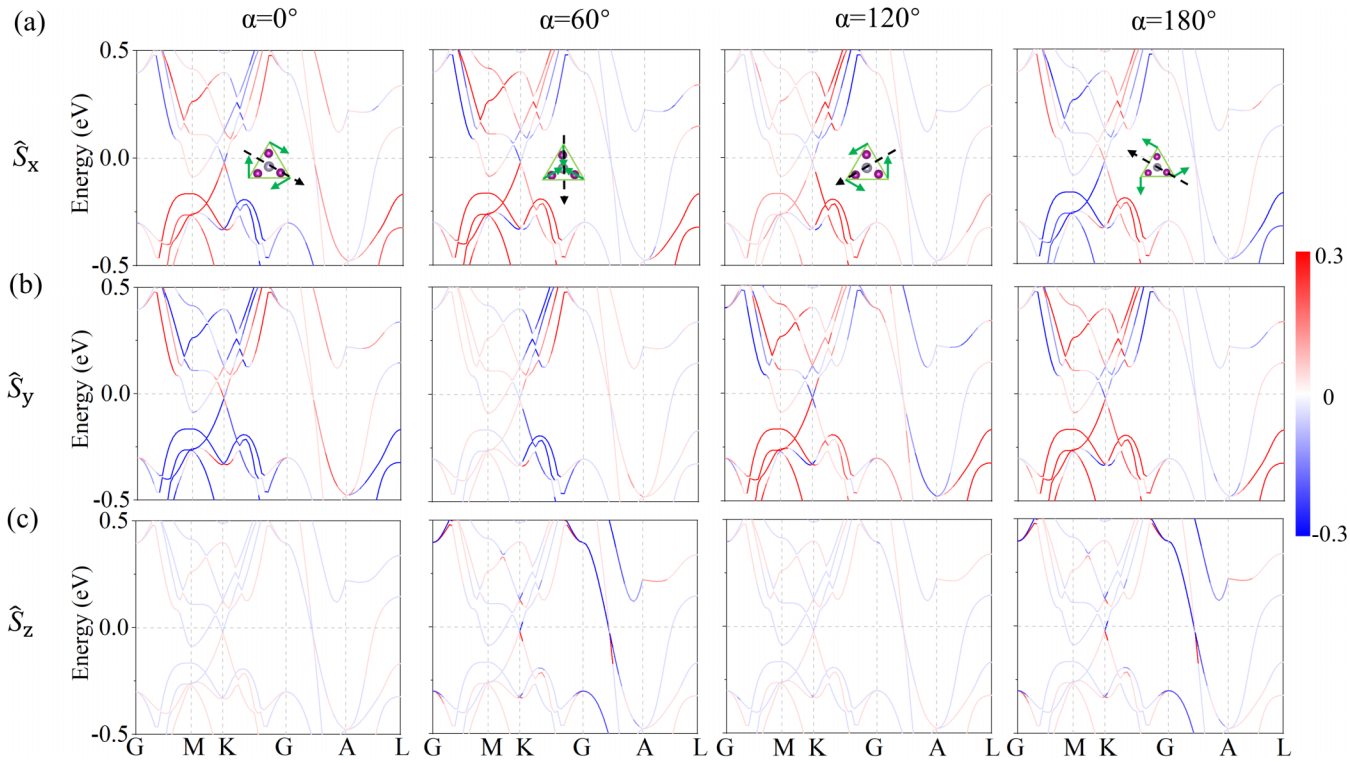

FIG. 3. The corresponding band structures of (a) $\hat{S}_x$, (b) $\hat{S}_y$, and (c) $\hat{S}_z$ of Mn_3Sn. The magnetic structure Néel vectors (black dashed arrows) orientation along clockwise rotation 0°, 60°, 120°, 180° of Mn_3Sn. The green arrows are magnetic structures. The figure displays the color scale of the spin values, indicating the direction and magnitude of the magnetic moment.

field which can be controlled by changing the direction of the applied electric field as shown in Fig. 2(b), and according to nudged elastic band (NEB) calculations, the switching barriers are lower than 0.12 eV so that the polarization can be reversibly switched. Furthermore, the band gap of α-In_2Se_3, approximately 0.8 eV, positions it as a suitable barrier layer.

As illustrated in Fig. 3, the Néel vector α can be used to define the nonlinear AFM order of bulk Mn_3Sn. Equal symmetric AFM states are indicated by four Néel vector directions, $\alpha = 0°$, 60°, 120°, and 180°. In quantum mechanics, the motion of spin is described by a wave function, and the spin component is represented by the expectation value of the wave function. We perform computations to investigate the band structure and the spin expectation values associated with each band for the four distinct nonlinear AFM states present in Mn_3Sn, given the spin-split nature of the band structure. As can be seen in Fig. 3, the spin expectation values change gradually with α from 0° to 180° for all bands. Interestingly, the in-plane spin components $\hat{S}_x$ and $\hat{S}_y$ demonstrate contrasting polarities at $\alpha = 0°$ and $\alpha = 180°$, suggesting that the inversion of the Néel vector bears resemblance to a time-reversal symmetry operation within the plane, while $\hat{S}_z$ does not exhibit a similar effect. This suggests that inversion in the direction of $\hat{S}_z$ does not have the same symmetry properties as the in-plane spin component. Specifically, $\hat{S}_z$ is the same at $\alpha = 0°$ and $\alpha = 120°$, and also at $\alpha = 60°$ and $\alpha = 180°$. This means that $\hat{S}_z$ has certain symmetry properties at the specific angle of 120°. Due to the spin splitting of the band structure, the change in the rotation angle α of the Néel vector affects the spin expectation value at each k point. This formula can be used to determine each Bloch state's spin expectation value:

$$\hat{S}i = \frac{\hbar}{2}\langle\psi_n(k)|\sigma_i|\psi_n(k)\rangle, \tag{1}$$

where $\hat{S}i$ denotes the expectation value of the spin in the i direction at each k point, $\hbar$ is the approximate Planck's constant, $\psi_n(k)$ is the Bloch wave function, and σ_i is the ith component of the Pauli matrix.

C. Multiple resistive state devices

In MFTJs, multiple resistive states can be realized by controlling the interaction between the ferroelectric and magnetic layers. A common method is to use the modulation of the polarization direction of the ferroelectric layer and the magnetic moment direction of the magnetic layer to achieve different resistive states. Typically, this method can yield four resistive states, and the number of resistive states can be further expanded by increasing the number of ferroelectric layer interfaces. However, increasing the number of layers of the ferroelectric layer increases the thickness of the device. This may give rise to several issues, including elevated device fabrication costs, augmented demand for a magnetic field to flip the magnetic moment. Therefore, the pursuit of achieving a greater number of resistive states without escalating the device thickness constitutes a pivotal challenge in MFTJs research.

The noncollinear AFM material Mn_3Sn has multiple Néel vector directions, which means that different resistive states can be realized by controlling the rotation of the magnetic

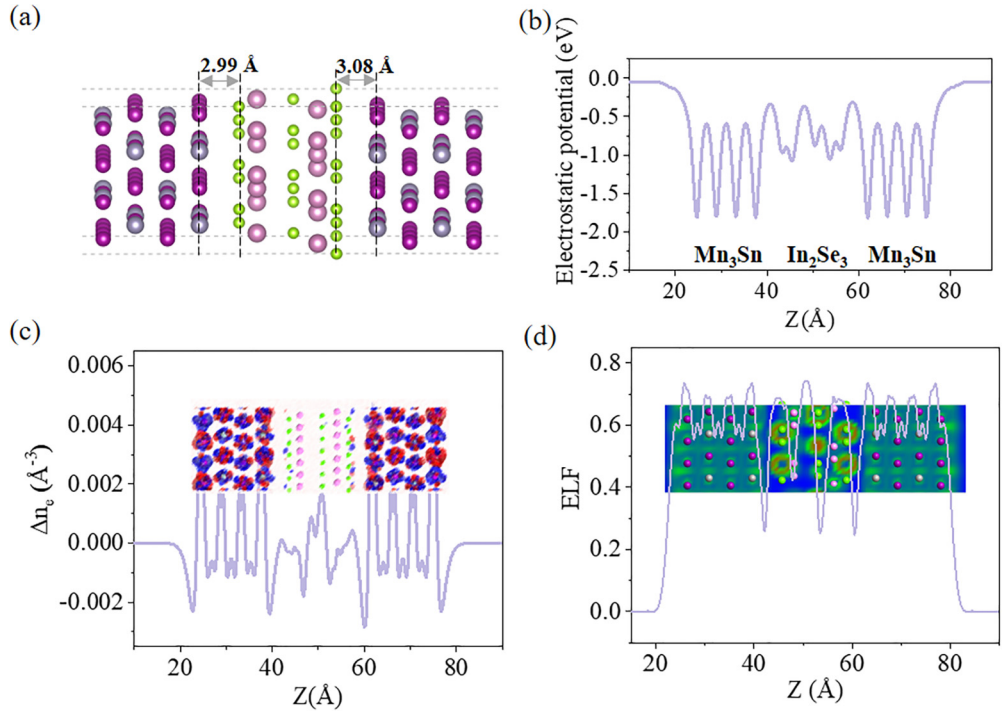

FIG. 4. (a) Atomic structure and (b) averaged electrostatic potential of the P← polarized in Mn_3Sn/α-In_2Se_3/Mn_3Sn. (c) Differential charge density distributions of the heterojunction. The red and blue isosurfaces indicate electron accumulation and depletion after layer stacking, respectively.

moment directions without increasing the number of layers. This approach allows more resistive states to be realized while reducing the thickness of the device, thereby improving the performance and application potential of the MFTJ. Figure 4(a) shows the atomic structure diagram of MFTJs with Mn_3Sn and α-In_2Se_3, the corresponding minimum lattice mismatch is 2.3%, and the Mn_3Sn and α-In_2Se_3 supercells are 2 × 2 and 3 × 3, respectively. Figure 4(b) shows the in-plane average electrostatic potentials of the Mn_3Sn/α-In_2Se_3/Mn_3Sn junction for the left (P←) polarized state of α-In_2Se_3. The retention of vertical polarization can be further elucidated by the charge distributions in Fig. 4(c), which shows evidence of interlayer inequivalence in the intermediate α-In_2Se_3 layers in the P← state. The electron localization function (ELF) is a tool for studying the electronic structure of materials. Within the materials, the ELF values for Mn_3Sn and α-In_2Se_3 are between 0.5 and 1 [see Fig. 4(d)], indicating that the electron distribution around the atomic nuclei is relatively localized, with electrons being more concentrated in specific regions. At the interfaces, the ELF values are between 0 and 0.5, which typically occurs in regions of nonbonding or lone pair electrons, indicating weaker electron localization and greater dispersion within these areas.

D. ELF of heterojunction

In Fig. 5(a), we first consider the four states of the Néel vector, device Mn_3Sn/α-In_2Se_3/Mn_3Sn, by rotating Mn_3Sn, which is shown schematically using unit cell-sized devices for a better display of the orientations. To analyze more fully how the magnetization arrangement of AFM affects electron transport, we calculate the $k_\parallel$ resolved transmission coefficients (T) of Mn_3Sn/α-In_2Se_3/Mn_3Sn MFTJ at the Fermi level in the two-dimensional (2D) Brillouin zone in Fig. 5(b). The probability of electron flow through the tunneling phenomenon is described by the Landauer-Büttiker formula in the framework of quantum mechanics:

$$G(E) = \frac{2e^2}{h}\sum_{k_\parallel} T(E, k_\parallel), \tag{2}$$

where $T(E, k_\parallel)$ is the transmission coefficient. The $k_\parallel = (k_x, k_y)$ is the Bloch wave vector corresponding to the junction plane. It relates the current density to the transmittance, which is the probability of an electron crossing the potential barrier from one region to another. The Landauer-Büttiker formula can be used to describe the probability of electron flow through a potential barrier, which is related to the height and width of the barrier as well as the energy of the electrons (the Fermi surface is shown in Fig. S2 in the Supplemental Material [47]). It can be observed that $T(k_\parallel)$ reaches its highest value when α_R is 0°, as shown in Fig. 5(b), and gradually decreases with increasing α_R in the range 0–180°. When $\alpha_R = 0°$, the bright spots of the $T(k_\parallel)$ are distributed around the Γ point, while the bright spots rotate as α_R gradually turns to 180°, while the extent of the 2D Brillouin zone gradually decreases, and the intensity of the bright spots is weakened. This is because the increase in α_R results in a spin mismatch between the electron wave incident from the left Mn_3Sn electrode and the electron wave output from the right Mn_3Sn electrode. Based on the $T(k_\parallel)$ in the 2D Brillouin zone in Fig. 5(b), it can be judged that the magnetoresistive states will be in the four states. However, it is possible that insufficient electron scattering resulted in a small difference

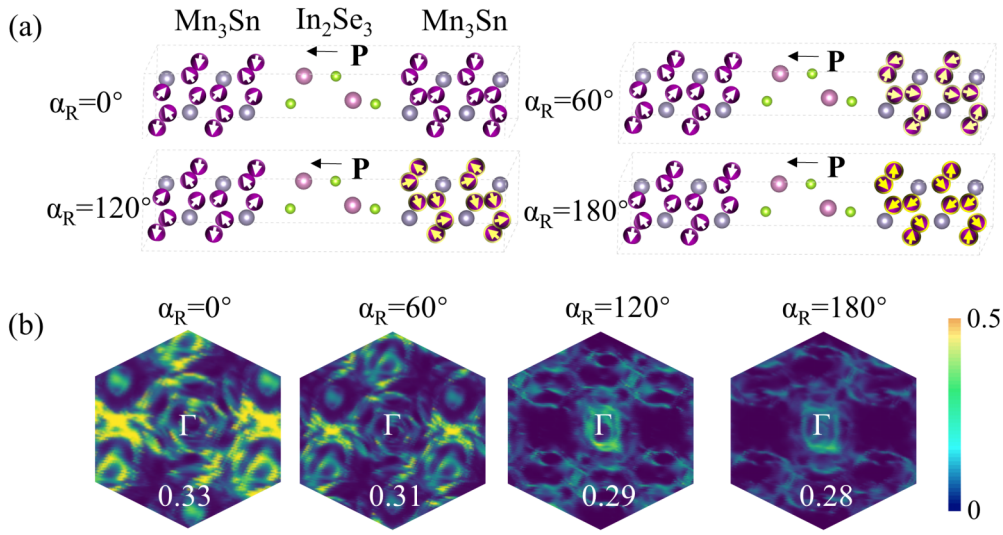

FIG. 5. (a) Schematic diagrams of the MFTJs structures of P ($\alpha_L = 0°$, $\alpha_R = 0°$) and AP ($\alpha_L = 0°$, $\alpha_R = 60°$; $\alpha_L = 0°$, $\alpha_R = 120°$; $\alpha_L = 0°$, $\alpha_R = 180°$). (b) The corresponding 2D Brillouin zone $k_{\|}$-resolved transmission coefficients of the MFTJs.

in transmission between the P and AP states, implying a small tunneling magnetoresistance (TMR) effect at this point. The TMR ratio can be calculated by

$$\mathrm{TMR} = \frac{T_P - T_{AP}}{T_{AP}}, \tag{3}$$

where T_P and T_P are the total transmission coefficient of the Fermi level junctions in P and AP magnetic states, respectively. We calculate a TMR of 18% in the Mn_3Sn/α-In_2Se_3/Mn_3Sn device; see Table S1 in the Supplemental Material [47].

For MFTJs, a left-right symmetric electrode would destroy the charge arrangement of the ferroelectric layer, resulting in a lower electrode polarization rate and thus a small TER. We insert a hexagonal BN layer on one side for charge shielding, which at the same time allows the electrons to scatter more fully in the device. We then construct the MFTJs of $Mn_3Sn/BN/\alpha$-In_2Se_3/Mn_3Sn in Fig. 6, in which the charge arrangement of the ferroelectric layer α-In_2Se_3 will be maintained in this device structure. The switchable built-in electric field within the α-In_2Se_3 layer can be seen from the potential distribution plots in Figs. 6(c) and 6(d), as shown by the yellow line in the figure. This observation confirms the presence of ferroelectric polarization in the α-In_2Se_3 interlayer, indicating the occurrence of the TER effect. When the BN layer interacts with the MFTJs, additional scattering centers

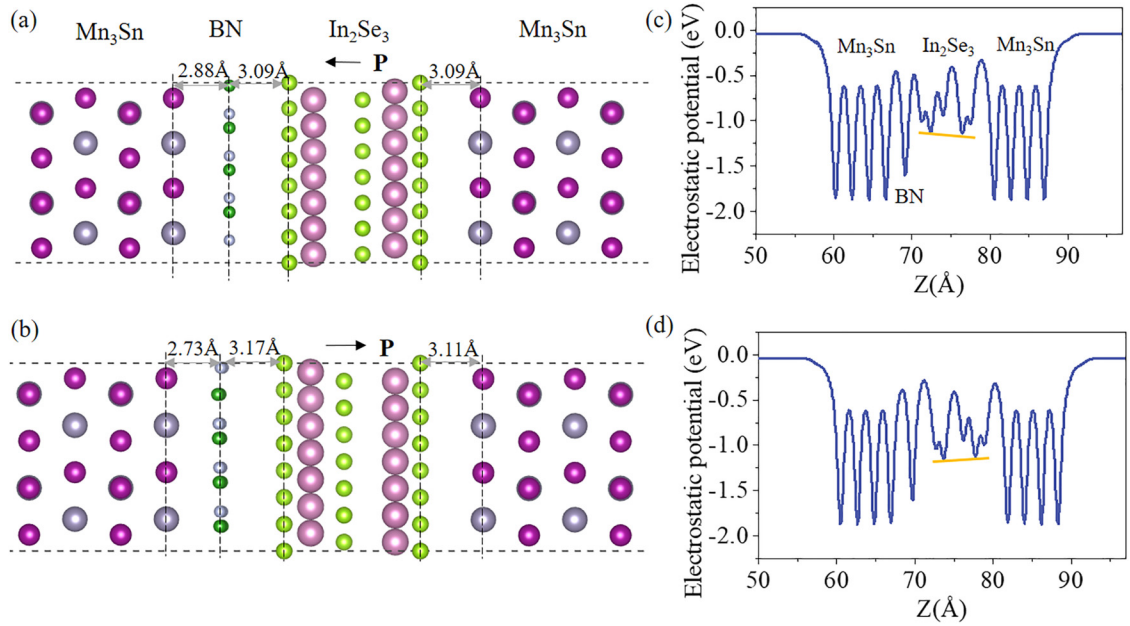

FIG. 6. Atomic structure diagram of $Mn_3Sn/BN/\alpha$-In_2Se_3/Mn_3Sn MFTJ of the P← state (a) and P→ state (b). The electrostatic potential of the transport direction z axis for the MFTJ of the P← state (c) and P→ state (d).

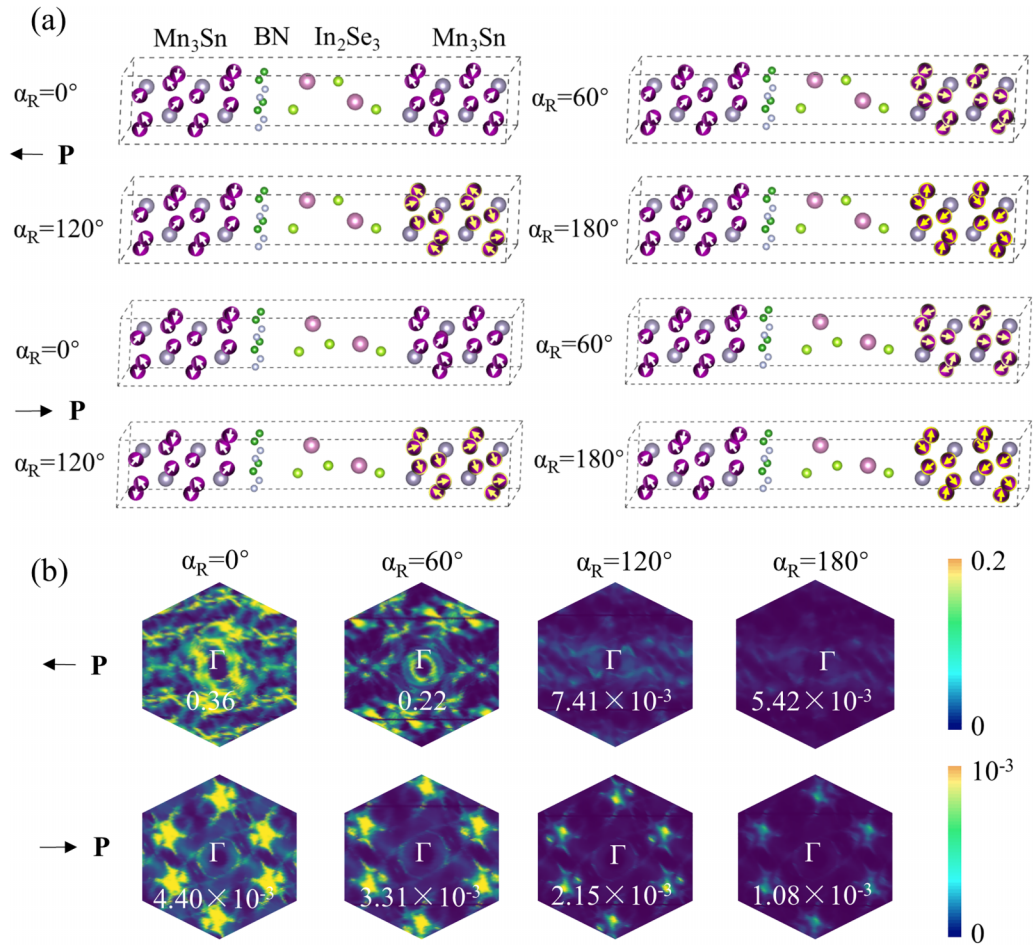

FIG. 7. (a) Schematic diagrams of the $Mn_3Sn/BN/\alpha$-In_2Se_3/Mn_3Sn structures of P ($\alpha_L = 0°$, $\alpha_R = 0°$) and AP ($\alpha_L = 0°$, $\alpha_R = 60°$; $\alpha_L = 0°$, $\alpha_R = 120°$; $\alpha_L = 0°$, $\alpha_R = 180°$). (b) The corresponding 2D Brillouin zone $k_\parallel$-resolved transmission coefficients intensities of the above eight configurations.

are introduced to increase the scattering of electrons, which reduces the transmission probability of the inverse flat form of the device and enhances the TMR effect.

Based on this, MFTJs with eight resistive states are constructed [Fig. 7(a)]. In the following, we explore four distinct Néel vector orientations of Mn_3Sn and two different ferroelectric polarization states of α-In_2Se_3. The specific operations are as follows: In MFTJs, keep the Néel vector direction of the left electrode Mn_3Sn unchanged, and rotate the Néel vector of the right electrode Mn_3Sn to 0°, 60°, 120°, and 180°, respectively. Then change the polarization direction of α-In_2Se_3 from the P← state to the P→ state, while rotating the Néel vector of the right electrode Mn_3Sn to 0°, 60°, 120°, and 180°. The mutual control of the Néel vector direction of the left and right electrodes Mn_3Sn and the polarization direction of α-In_2Se_3 will result in eight different configurations of MFTJs, as shown in Fig. 7(a). With the α-In_2Se_3 polarization to the left, the electron transmittance is larger when the α_R is set at 0° [Fig. 7(b)]. When the α_R is equal to 180°, the electron transmittance around the interior of the Brillouin zone decreases significantly, and the significantly different conductivities of the four magnetic structures lead to the obvious TMR effect in the MFTJs. Furthermore, comparing MFTJs with different ferroelectric polarization directions (P→ and P←), it is evident that the electron transmission coefficients for the P→ state and the P← state exhibit significant differences. In particular, substantial differences in the order of magnitude are observed at $\alpha_R = 0°$ and $\alpha_R = 60°$, resulting in a considerable TER ratio.

Table I summarizes the electron transmission, as well as the TMR and TER ratios calculated for the $Mn_3Sn/BN/\alpha$-In_2Se_3/Mn_3Sn MFTJs. TER ratio is defined as

$$\mathrm{TER} = \frac{|T_{p\leftarrow} T_{p\rightarrow}|}{\min(T_{p\leftarrow}, T_{p\rightarrow})}, \tag{4}$$

where $T_{p\leftarrow/p\rightarrow}$ is the total transmission coefficient at the Fermi level which can be obtained by reversing the direction of the ferroelectric polarization of the barrier layer. It is noteworthy that, in comparison to the symmetric Mn_3Sn/α-In_2Se_3/Mn_3Sn MFTJs configuration, a notable increase in the TMR ratio is observed, reaching as high as 6650%. This enhancement can be attributed to a more pronounced attenuation of transmission in the AP state relative to the P state. Additionally, the asymmetric MFTJs with the BN interface have a significant impact on the ferroelectric control of resistance in the MFTJs. In the P magnetization alignment, the corresponding TER ratio can exceed 8180%. When the MFTJ is in the P← state, the T changes from 0.36 to 5.42×10^{-3} as α_R varies

TABLE I. The transmission coefficient (T) and resistive area [RA ($\Omega\,\mu\mathrm{m}^2$) $= A/G$, where A is the area of the unit cell and G (e^2/h) is the conductance] for different Néel vectors. The resistive value is represented by each state. The TMR and TER of $Mn_3Sn/BN/\alpha$-In_2Se_3/Mn_3Sn MFTJ.

	$\alpha_R = 0^\circ$		$\alpha_R = 60^\circ$		$\alpha_R = 120^\circ$		$\alpha_R = 180^\circ$		
	T	RA	T	RA	T	RA	T	RA	TMR (%)
P←	0.36	6.94×10^{-2}	0.22	5.68×10^{-2}	7.41×10^{-3}	3.37	5.42×10^{-3}	4.61	6.65×10^{3}
Resistive states	(111)		(110)		(101)		(100)		
P→	4.40×10^{-3}	5.68	3.31×10^{-3}	7.55	2.15×10^{-3}	1.16×10^{1}	1.08×10^{-3}	2.31×10^{1}	3.07×10^{2}
Resistive states	(011)		(010)		(001)		(000)		
TER (%)	8.18×10^{3}		6.55×10^{3}		2.45×10^{2}		4.02×10^{2}		

from 0° to 180°. Similarly, in the P→ state, the T changes from 4.40×10^{-3} to 1.08×10^{-3} over the same range of α_R values. These eight distinct Ts correspond to the stepped magnetoresistance distribution pattern proposed in Fig. 1. The state with the highest T, corresponding to the P← state at $\alpha_R = 0^\circ$, is defined as "111," while the state with the lowest T, corresponding to the P→ state at $\alpha_R = 180^\circ$, is defined as "000," with the remaining states arranged accordingly. After rotating the antiferromagnetic Néel vector and changing the polarization direction, MFTJ achieves control of eight resistance states, which can be used in the field of information storage.

III. CONCLUSIONS

In summary, we have analyzed in detail the structural properties of the spin-splitting bands in Mn_3Sn, a representative noncollinear AFM metal, through first-principles calculations. Furthermore, we have successfully predicted the existence of eight distinct resistive states in the $Mn_3Sn/BN/\alpha$-In_2Se_3/Mn_3Sn MFTJs, in which the TMR ratio and TER ratio could exceed 1000%. These findings not only contribute to a deeper understanding of the behavior of noncollinear AFM metals but also offer valuable insight into their potential applications as MFTJ electrodes in AFM spintronics. This has significant implications for the development of storage technology, as it demonstrates the feasibility of utilizing AFM materials to enhance spintronic devices and advance the field of data storage and processing.

ACKNOWLEDGMENTS

This work was supported by National Key R&D Program of China (Grant No. 2018YFA0703700), the National Natural Science Foundation of China (Grants No. U23A20364, No. 62104172, and No. 62104171), and the Strategic Priority Research Program of Chinese Academy of Sciences (Grant No. XDB44000000). The numerical calculations in this paper were performed on the supercomputing system in the Supercomputing Center of Wuhan University [48].

[1] G. Sanchez-Santolino, J. Tornos, D. Hernandez-Martin, J. I. Beltran, C. Munuera, M. Cabero, A. Perez-Muñoz, J. Ricote, F. Mompean, M. Garcia-Hernandez, Z. Sefrioui, C. Leon, S. J. Pennycook, M. C. Muñoz, M. Varela, and J. Santamaria, Resonant electron tunnelling assisted by charged domain walls in multiferroic tunnel junctions, Nat. Nanotechnol. **12**, 655 (2017).

[2] L. Yin, R. Cheng, Y. Wen, C. Liu, and J. He, Emerging 2D memory devices for in-memory computing, Adv. Mater. **33**, 2007081 (2021).

[3] L. N. Jiang, Y.-P. Wang, Y. Zhu, and X. F. Han, Enhanced tunneling electroresistance effect by designing interfacial ferroelectric polarization in multiferroic tunnel junctions, Phys. Rev. B **105**, 134410 (2022).

[4] A. Xie, H. Hao, C.-S. Liu, X. Zheng, L. Zhang, and Z. Zeng, Giant tunnel electroresistance in two-dimensional ferroelectric tunnel junctions constructed with a Sc_2CO_2/In_2Se_3 van der Waals ferroelectric heterostructure, Phys. Rev. B **107**, 115427 (2023).

[5] Y. Su, X. Li, M. Zhu, J. Zhang, L. You, and E. Y. Tsymbal, Van der Waals multiferroic tunnel junctions, Nano. Lett. **21**, 175 (2020).

[6] G. Dastgeer, S. Nisar, A. Rasheed, K. Akbar, V. D. Chavan, D.-k. Kim, S. M. Wabaidur, M. W. Zulfiqar, and J. Eom, Atomically engineered, high-speed non-volatile flash memory device exhibiting multibit data storage operations, Nano Energy **119**, 109106 (2024).

[7] X. Dong, X. Shen, X. Sun, Y. Bai, Z. Yan, and X. Xu, Voltage-tunable giant nonvolatile multiple-state resistance in sliding-interlayer ferroelectric h−BN van der Waals multiferroic tunnel junction, Phys. Rev. B **108**, 085427 (2023).

[8] S. Li, Z. Zhang, X. Chen, W. Deng, Y. Lu, M. Sui, F. Gong, G. Xu, X. Li, F. Liu, C. You, F. Chu, Y. Wu, H. Yan, and Y. Zhang, A high-performance in-memory photodetector realized by charge storage in a van der Waals MISFET, Adv. Mater. **34**, 2107734 (2022).

[9] W. Huang, F. Wang, L. Yin, R. Cheng, Z. Wang, M. G. Sendeku, J. Wang, N. Li, Y. Yao, and J. He, Gate-coupling-enabled robust hysteresis for nonvolatile memory and programmable rectifier in van der Waals ferroelectric heterojunctions, Adv. Mater. **32**, 1908040 (2020).

[10] H. Wang, Y. Wen, H. Zeng, Z. Xiong, Y. Tu, H. Zhu, R. Cheng, L. Yin, J. Jiang, B. Zhai, C. Liu, C. Shan, and J. He, Two-dimensional ferroic materials for non-volatile memory applications, Adv. Mater. 2305044 (2023).

[11] A. Hirohata, MRAM makes its mark, Nat. Electron. **5**, 832 (2022).

[12] T. Song, X. Cai, Matisse W. Tu, X. Zhang, B. Huang, N. P. Wilson, K. L. Seyler, L. Zhu, T. Taniguchi, K. Watanabe, M. A. McGuire, D. H. Cobden, D. Xiao, W. Yao, and X. Xu, Giant tunneling magnetoresistance in spin-filter van der Waals heterostructures, Science **360**, 1214 (2018).

[13] S. Yuasa, T. Nagahama, and Y. Suzuki, Spin-polarized resonant tunneling in magnetic tunnel junctions, Science **297**, 234 (2002).

[14] J. Chen, G. Dun, J. Hu, Z. Lin, Y. Wang, T. Lu, P. Li, T. Wei, J. Zhu, J. Wang, X. Li, X.-M. Wu, Y. Yang, and T.-L. Ren, Polarized tunneling transistor for ultrafast memory, ACS Nano **17**, 12374 (2023).

[15] S. Jung, H. Lee, S. Myung, H. Kim, S. K. Yoon, S.-W. Kwon, Y. Ju, M. Kim, W. Yi, S. Han, B. Kwon, B. Seo, K. Lee, G.-H. Koh, K. Lee, Y. Song, C. Choi, D. Ham, and S. J. Kim, A crossbar array of magnetoresistive memory devices for in-memory computing, Nature (London) **601**, 211 (2022).

[16] J. Shen, W. Song, K. Ren, Z. Song, P. Zhou, and M. Zhu, Toward the speed limit of phase-change memory, Adv. Mater. **35**, 2208065 (2023).

[17] U. Chon, H. M. Jang, M. G. Kim, and C. H. Chang, Layered perovskites with giant spontaneous polarizations for nonvolatile memories, Phys. Rev. Lett. **89**, 087601 (2002).

[18] H. Shen, J. Liu, K. Chang, and L. Fu, In-plane ferroelectric tunnel junction, Phys. Rev. Appl. **11**, 024048 (2019).

[19] Y. Li, L. Loh, S. Li, L. Chen, B. Li, M. Bosman, and K.-W. Ang, Anomalous resistive switching in memristors based on two-dimensional palladium diselenide using heterophase grain boundaries, Nat. Electron. **4**, 348 (2021).

[20] N. Ding, K. Yananose, C. Rizza, F.-R. Fan, S. Dong, and A. Stroppa, Magneto-optical Kerr effect in ferroelectric antiferromagnetic two-dimensional heterostructures, ACS Appl. Mater. Inter. **15**, 22282 (2023).

[21] L. Yin, X. Wang, and W. Mi, Ferromagnetic, ferroelectric, and optical modulated multiple resistance states in multiferroic tunnel junctions, ACS Appl. Mater. Inter. **11**, 1057 (2018).

[22] M. Fiebig, T. Lottermoser, D. Meier, and M. Trassin, The evolution of multiferroics, Nat. Rev. Mater. **1**, 1 (2016).

[23] X. Chen, S. Shi, G. Shi, X. Fan, C. Song, X. Zhou, H. Bai, L. Liao, Y. Zhou, H. Zhang, A. Li, Y. Chen, X. Han, S. Jiang, Z. Zhu, H. Wu, X. Wang, D. Xue, H. Yang, and F. Pan, Observation of the antiferromagnetic spin Hall effect, Nat. Mater. **20**, 800 (2021).

[24] S. Ghara, E. Barts, K. Vasin, D. Kamenskyi, L. Prodan, V. Tsurkan, I. Kézsmárki, M. Mostovoy, and J. Deisenhofer, Magnetization reversal through an antiferromagnetic state, Nat. Commun. **14**, 5174 (2023).

[25] T. Jungwirth, X. Marti, P. Wadley, and J. Wunderlich, Antiferromagnetic spintronics, Nat. Nanotechnol. **11**, 231 (2016).

[26] H. Wioland, F. G. Woodhouse, J. Dunkel, and R. E. Goldstein, Ferromagnetic and antiferromagnetic order in bacterial vortex lattices, Nat. Phys. **12**, 341 (2016).

[27] C. Marrows, Addressing an antiferromagnetic memory, Science **351**, 558 (2016).

[28] P. Qin, H. Yan, X. Wang, H. Chen, Z. Meng, J. Dong, M. Zhu, J. Cai, Z. Feng, X. Zhou, L. Liu, T. Zhang, Z. Zeng, J. Zhang, C. Jiang, and Z. Liu, Room-temperature magnetoresistance in an all-antiferromagnetic tunnel junction, Nature (London) **613**, 485 (2023).

[29] D.-F. Shao, S.-H. Zhang, G. Gurung, W. Yang, and E. Y. Tsymbal, Nonlinear anomalous Hall effect for Néel vector detection, Phys. Rev. Lett. **124**, 067203 (2020).

[30] S. Ghosh, A. Manchon, and J. Železný, Unconventional robust spin-transfer torque in noncollinear antiferromagnetic junctions, Phys. Rev. Lett. **128**, 097702 (2022).

[31] J. Dong, X. Li, G. Gurung, M. Zhu, P. Zhang, F. Zheng, E. Y. Tsymbal, and J. Zhang, Tunneling magnetoresistance in noncollinear antiferromagnetic tunnel junctions, Phys. Rev. Lett. **128**, 197201 (2022).

[32] G. Gurung, D.-F. Shao, and E. Y. Tsymbal, Spin-torque switching of noncollinear antiferromagnetic antiperovskites, Phys. Rev. B. **101**, 140405(R) (2020).

[33] Q. Cao, W. Lü, X. R. Wang, X. Guan, L. Wang, S. Yan, and T. Wu, and X. Wang, Nonvolatile multistates memories for high-density data storage, ACS Appl. Mater. Inter. **12**, 42449 (2020).

[34] Y. Guo, B. Peng, R. Qiu, G. Dong, Y. Yao, Y. Zhao, Z. Zhou, and M. Liu, Self-rolling-up enabled ultrahigh-density information storage in freestanding single-crystalline ferroic oxide films, Adv. Funct. Mater. **33**, 2213668 (2023).

[35] A. Nisar, S. Dhull, S. Mittal, and B. K. Kaushik, SOT and STT-Based 4-bit MRAM cell for high-density memory applications, IEEE Trans. Electron. Dev. **68**, 4384 (2021).

[36] Q. Sun, M. Yuan, R. Wu, Y. Miao, Y. Yuan, Y. Jing, Y. Qu, X. Liu, and J. Sun, A light-programmed rewritable lattice-mediated multistate memory for high-density data storage, Adv. Mater. **35**, 2302318 (2023).

[37] H. C. Zhao, H. Xia, S. Hu, Y. Y. Lv, Z. R. Zhao, J. He, E. Liang, G. Ni, L. Y. Chen, X. P. Qiu, S. M. Zhou, and H. B. Zhao, Large ultrafast-modulated Voigt effect in noncollinear antiferromagnet Mn_3Sn, Nat. Commun. **12**, 5266 (2021).

[38] X. Li, C. Collignon, L. Xu, H. Zuo, A. Cavanna, U. Gennser, D. Mailly, B. Fauqué, L. Balents, Z. Zhu, and K. Behnia, Chiral domain walls of Mn_3Sn and their memory, Nat. Commun. **10**, 3021 (2019).

[39] S. Li, M. Huang, H. Lu, N. J. McLaughlin, Y. Xiao, J. Zhou, E. E. Fullerton, H. Chen, H. Wang, and C. R. Du, Nanoscale magnetic domains in polycrystalline Mn_3Sn films imaged by a scanning single-spin magnetometer, Nano. Lett. **23**, 5326 (2023).

[40] B. K. Hazra, B. Pal, J.-C. Jeon, R. R. Neumann, B. Göbel, B. Grover, H. Deniz, A. Styervoyedov, H. Meyerheim, I. Mertig, S.-H. Yang, and S. S. P. Parkin, Generation of out-of-plane polarized spin current by spin swapping, Nat. Commun. **14**, 4549 (2023).

[41] T. Higo, K. Kondou, T. Nomoto, M. Shiga, S. Sakamoto, X. Chen, D. Nishio-Hamane, R. Arita, Y. Otani, S. Miwa, and S. Nakatsuji, Perpendicular full switching of chiral antiferromagnetic order by current, Nature (London) **607**, 474 (2022).

[42] J. Y. Chauleau, T. Chirac, S. Fusil, V. Garcia, W. Akhtar, J. Tranchida, P. Thibaudeau, I. Gross, C. Blouzon, A. Finco, M. Bibes, B. Dkhil, D. D. Khalyavin, P. Manuel, V. Jacques, N. Jaouen, and M. Viret, Electric and antiferromagnetic chiral textures at multiferroic domain walls, Nat. Mater. **19**, 386 (2019).

[43] X. Yu, X. Zhang, and J. Wang, Fully electrically controlled van der Waals multiferroic tunnel junctions, ACS Nano **17**, 25348 (2023).

[44] Q. Zhang, X. Li, and J. Zhu, Direct observation of interface-dependent multidomain state in the $BaTiO_3$ tunnel barrier of a

multiferroic tunnel junction memristor, ACS Appl. Mater. Inter. **13**, 43641 (2021).

[45] X. Chen, T. Higo, K. Tanaka, T. Nomoto, H. Tsai, H. Idzuchi, M. Shiga, S. Sakamoto, R. Ando, H. Kosaki, T. Matsuo, D. Nishio-Hamane, R. Arita, S. Miwa, and S. Nakatsuji, Octupole-driven magnetoresistance in an antiferromagnetic tunnel junction, Nature (London) **613**, 490 (2023).

[46] T. Yu, R. Liu, Y. Peng, P. Zheng, G. Wang, X. Ma, Z. Yuan, and Z. Yin, Correlated electronic structure of the kagome metal Mn_3Sn, Phys. Rev. B **106**, 205103 (2022).

[47] See Supplemental Material at http://link.aps.org/supplemental/10.1103/PhysRevB.110.024428 for the calculation details; the electrostatic potential and structure of α-In_2Se_3; the Fermi surface of Mn_3Sn; the transmission coefficient and resistive area of $Mn_3Sn/In_2Se_3/Mn_3Sn$. It also contains Refs. [48–51].

[48] V. Wang, N. Xu, J. C. Liu, G. Tang, and W. T. Geng, VASPKIT: A user-friendly interface facilitating high-throughput computing and analysis using VASP code, Comput. Phys. Commun. **267**, 108033 (2021).

[49] G. Kresse and J. Furthmüller, Efficient iterative schemes for *ab initio* total-energy calculations using a plane-wave basis set, Phys. Rev. B **54**, 11169 (1996).

[50] J. P. Perdew and A. Zunger, Self-interaction correction to density-functional approximations for many-electron systems, Phys. Rev. B **23**, 5048 (1981).

[51] J. P. Perdew, K. Burke, and M. Ernzerhof, Generalized gradient approximation made simple, Phys. Rev. Lett **77**, 3865 (1996).